FRONTIERS OF PHYSICS

RESEARCH ARTICLE
Volume 21 / Issue 11 / 114202 / 2026

High-performance type-II BiOI/CdS heterojunction photodetector for ultraviolet imaging and optical communication

Haoyue Wei[1], Qiuhong Tan[1,2,†], Ran Ma[1], Peizhi Yang[3], Yingkai Liu[1,2], Qianjin Wang[1,2,‡]

1 College of Physics and Electronic Information, Yunnan Normal University, Kunming 650500, China
2 Yunnan Provincial Key Laboratory for Photoelectric Information Technology, Yunnan Normal University, Kunming 650500, China
3 Key Laboratory of Advanced Technique & Preparation for Renewable Energy Materials, Ministry of Education, Yunnan Normal University, Kunming 650500, China
Corresponding authors. E-mail: †tanqiuhong1@126.com, ‡qjwang@xtu.edu.cn
Received December 30, 2025; accepted March 13, 2026

ABSTRACT

Bismuth oxyiodide (BiOI), a ternary halide oxide with a tunable bandgap and strong UV-visible light absorption, has attracted significant attention for applications in photocatalysis, solar cells, and photodetection. However, its relatively low photocurrent and sluggish photoresponse limit its practical use in high-performance photodetectors. To overcome these challenges, a BiOI/CdS heterojunction photodetector was designed and fabricated, featuring a type-II band alignment to enhance charge separation efficiency. Under ultraviolet illumination (300 nm), the device exhibited an exceptionally high on/off current ratio of 1.82×10^7, rapid response and recovery times of 72 μs and 244 μs, respectively, a responsivity of 1.54×10^4 A/W, an external quantum efficiency (EQE) of 6.37×10^6 %, and a specific detectivity of 4.08×10^{14} Jones. These outstanding optoelectronic characteristics highlight the great potential of the BiOI/CdS heterostructure for advanced ultraviolet (UV) imaging and optical communication systems, offering a promising route for the design of next-generation BiOI-based optoelectronic devices.

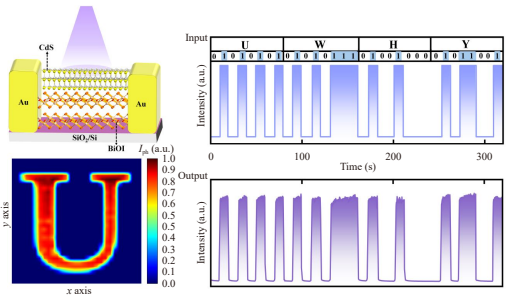

Keywords BiOI, heterojunction, optoelectronic characteristics, ultraviolet imaging, optical communication

1 Introduction

In recent years, two-dimensional (2D) materials have emerged as promising candidates for optoelectronic detection owing to their unique crystal structures, atomic thickness, and outstanding electronic and optical properties [1, 2]. Their tunable band structures and strong light-matter interactions offer significant potential for developing next-generation photodetectors with high sensitivity, fast response, and low energy consumption [3]. While early studies predominantly focused on single- or binary-element 2D materials, the discovery and synthesis of ternary 2D materials such as $NiPS_3$ [4], $InSiTe_3$ [5], and Bi_2O_2Se [6] have greatly expanded the material library for optoelectronic applications, providing additional opportunities for band engineering and performance optimization.

Among various ternary 2D materials, bismuth oxyhalides (BiOX, X = Cl, Br, I) have attracted widespread attention due to their tunable bandgap, strong light absorption, high environmental stability, and low toxicity [7]. These materials have been successfully

https://doi.org/10.15302/frontphys.2026.114202

applied in photocatalysis, memristive devices, photodetectors, and solar cells [8–12]. Particularly, BiOI has shown great potential in photodetection owing to its moderate bandgap (~2.2 eV) [13] and excellent absorption capability in the UV-visible region. However, the intrinsic low carrier mobility of BiOI limits its practical photodetector performance, resulting in low photocurrent, limited responsivity [14], and relatively slow response times (typically in the millisecond range) [15].

To overcome these limitations, constructing heterojunction structures with suitable band alignment has been recognized as an effective strategy to enhance charge separation and boost photoresponse. This strategy has been widely validated in various photodetector material systems. Taking the research on graphene-based heterojunctions (graphene/HgCdTe, graphene/ZnO) as an example, these studies have provided critical insights into high-performance heterojunction engineering, demonstrating that efficient charge separation and internal gain can be achieved through interfacial band engineering [16–18]. Among numerous 2D semiconductors, cadmium sulfide (CdS) has drawn particular interest due to its appropriate bandgap (2.4 eV) [19], high electron mobility, low work function, and excellent photosensitivity [20, 21]. Previous reports have demonstrated BiOI/CdS heterojunctions in photocatalytic systems, typically featuring flower-like or microsphere morphologies and exhibiting a type-II band structure that promotes spatial separation of photogenerated carriers [22, 23]. Nevertheless, research on BiOI/CdS heterostructures for photodetection remains scarce, especially concerning low-dimensional morphologies such as nanosheets and nanoribbons, which could offer superior interfacial contact and enhanced photoelectric performance.

In this study, we successfully fabricated BiOI nanosheets via a chemical vapor deposition (CVD) confinement method, and subsequently constructed BiOI/CdS heterojunction photodetectors using a dry transfer process. The photoelectric properties of the heterostructure were systematically investigated under ultraviolet irradiation (300 nm). The device exhibited exceptional optoelectronic performance, achieving an ultra-high switching current ratio (1.82×10^7), high responsivity (1.54×10^4 A/W), high external quantum efficiency (6.37×10^{6}%), high specific detectivity (4.08×10^{14} Jones), and a rapid response time (72 μs/244 μs). Moreover, kelvin probe force microscopy (KPFM) and photocurrent mapping analyses confirmed effective charge transfer across the heterojunction interface. Leveraging its superior sensitivity and fast optical response, the device is further demonstrated in UV imaging and optical communication, underscoring its promising potential for future integrated optoelectronic applications.

2 Experimental section

2.1 Synthesis of BiOI nanosheets

BiOI nanosheets were synthesized via a spatially confined growth method. Layered mica was first mechanical exfoliation, and BiI_3 powder (Aladdin, 99.99%) was placed between two freshly cleaved mica sheets. The assembled structure was clamped between glass slides to enhance spatial confinement and then placed at the center of a single-zone tube furnace. The growth was carried out at atmospheric pressure and a temperature range of 370–400 °C for 5 minutes. After natural cooling to room temperature, the BiOI nanosheets were successfully obtained.

2.2 Transfer of BiOI nanosheets

The mica substrate containing as-grown BiOI nanosheets was spin-coated with a polystyrene (PS) solution at 2800 rpm for 40 seconds and subsequently baked at 55 °C for 5 minutes. The coated sample was then cut into small pieces and immersed in deionized water. Driven by surface tension, the PS/BiOI composite film detached from the mica and floated on the water surface. The floating film was carefully scooped onto a SiO_2/Si wafer, baked again at 55 °C for 10 minutes, and finally immersed in toluene to dissolve the PS layer, leaving the BiOI nanosheets firmly adhered to the target substrate. A schematic illustration of this process is provided in Fig. S1.

2.3 Preparation of CdS nanobelts

Silicon dioxide substrates (1.5×1.5 cm^2) were sequentially cleaned in acetone, ethanol, and deionized water for 10 minutes each, followed by nitrogen drying. A thin gold (Au) film was subsequently deposited on the silicon substrates via sputtering. For CdS nanobelt growth, a quartz boat containing CdS powder (Mackin, 99.999%) was positioned at the center of a single-zone tube furnace, while the Au-coated silicon substrate was placed 15 cm downstream from the source. Prior to heating, the system was evacuated to achieve a low-pressure environment. High-purity argon gas was introduced at 200 sccm for 15 minutes to purge the tube and minimize contamination. The gas flow was then reduced to 100 sccm, and the furnace temperature was raised to 850 °C and maintained for 2 hours. After completion, the furnace was naturally cooled to room temperature under continuous argon flow. A fluffy yellow product was collected from the substrate and dispersed in ethanol for subsequent use. A schematic of the growth setup is shown in Fig. S2.

2.4 Fabrication of BiOI/CdS heterojunction device

The BiOI nanosheets on SiO_2/Si substrates were patterned using ultraviolet (UV) photolithography to define electrode regions. The process involved spin-coating photoresist (AZ5214), soft baking at 80 °C, UV exposure for 8 seconds, and development in AZ300MIF for 15 seconds. Ti/Au (5 nm/18 nm) electrodes were then deposited by thermal evaporation. CdS nanobelts, dispersed in ethanol, were drop-cast onto a SiO_2/Si wafer and subsequently transferred onto the target BiOI nanosheets using a PMMA-assisted dry transfer technique. Finally, the heterojunction device was annealed at 120 °C for 10 minutes to improve interfacial contact.

2.5 Characterizations

The morphology and crystal structure of BiOI nanosheets were characterized using SEM (Scientific Escalab 250), XRD (DX-2700), XPS (Thermo Fisher Scientific K-Alpha), EDS (Scientific Escalab 250), Raman spectroscopy (LabRam HR Evolution), and PL spectroscopy (IK3301). The absorption curve of BiOI was characterized using an ultraviolet-near infrared (UV-NIR) micro-absorption spectroscopy system (MStarter ABS). The thickness and surface potential of the material were investigated using a scanning probe microscope (Dimenson ICON) equipped with AFM and KPFM modules. The photodetection performance of the fabricated photodetectors was measured using a semiconductor integrated test system (Keithley 4200-SCS) connected to a probe station. The device's response time, single-point imaging, and scanning photocurrent mapping were measured using the Mstarter 200 (Metatest Corporation, China) high-precision photocurrent scanning test microscope.

3 Results and discussion

Figure 1(a) illustrates the synthesis process of BiOI nanosheets via the space-confinement method. In this approach, BiI_3 is sandwiched between two mica sheets, forming a narrow interlayer gap that serves as a confined micro-reactor for crystal growth. This spatial restriction effectively slows the crystal growth rate of BiOI, enabling the controlled formation of few-layer BiOI nanosheets [24, 25]. The resulting BiOI exhibits a layered crystal structure composed of alternating bismuth–oxygen ($[Bi_2O_2]^{2+}$) and iodide (I^-) layers that crystallize in a tetragonal lattice belonging to the P4/nmm space group [26], as shown in Fig. 1(b). Figure 1(c) presents an optical microscopy image of BiOI nanosheets grown on a mica substrate. The uniform and smooth surface morphology reveals the high crystalline quality of the as-synthesized nanosheets. Complementary scanning electron microscopy (SEM) and energy-dispersive X-ray Spectroscopy (EDS) further confirm the uniform spatial distribution of Bi, O, and I elements across the nanosheet (Fig. S3), validating the homogeneous composition of BiOI.

The X-ray diffraction (XRD) pattern in Fig. 1(d) displays sharp diffraction peaks located at approximately 9.61°, 19.36°, 39.38°, and 49.83°, which can be indexed to the (001), (002), (004), and (005) planes of tetragonal BiOI, respectively. These peaks are in excellent agreement with the standard JCPDS card No. 73-2062, confirming the high phase purity and crystallinity of the sample. Notably, the absence of non-(00l) peaks indicates that the BiOI nanosheets preferentially grow along the [001] orientation, while several additional strong peaks originate from the mica substrate. The optical properties of BiOI were further examined using ultraviolet-visible (UV-Vis) absorption spectroscopy [Fig. 1(e)]. BiOI, as an indirect band-gap semiconductor, follows the Tauc relation $(\alpha h\nu)^{0.5}=(h\nu-E_g)$ [27]. The inset in Fig. 1(e) shows a band gap of approximately 2.02 eV, which is in close agreement with the theoretical value of 2.2 eV [13]. The X-ray photoelectron spectroscopy (XPS) spectra provide detailed insights into the elemental composition and chemical states (Fig. S4). The Bi 4f spectrum displays two distinct peaks at 164.3 eV and 159.0 eV, corresponding to the $4f_{5/2}$ and $4f_{7/2}$ states of Bi^{3+}, with a splitting of 5.3 eV. In the I 3d spectrum, peaks observed at 630.5 eV and 618.9 eV are attributed to I $3d_{3/2}$ and I $3d_{5/2}$, respectively [28]. The O 1s peak at 530.0 eV, after accounting for the oxygen contribution from the mica substrate, is assigned to oxygen in BiOI. These results align well with previously reported XPS data [15].

Figure 1(f) shows the Raman spectra of the BiOI/CdS heterostructure. The BiOI nanosheets exhibit characteristic Raman peaks at 87 cm^{-1} and 152 cm^{-1}, corresponding to A_{1g} and E_g phonon modes associated with Bi-I vibrations [29]. The Raman spectrum of CdS presents two pronounced peaks at 302 cm^{-1} and 602 cm^{-1}, which correspond to the 1LO and its second-order 2LO phonon modes. The Raman spectrum of the BiOI/CdS stacked region exhibits all characteristic peaks of BiOI and CdS, confirming the successful formation of a heterojunction without noticeable peak shifts, indicative of a high-quality interface. The photoluminescence (PL) spectra in Fig. 1(g) further support this conclusion. Compared to pristine CdS, the BiOI/CdS heterojunction shows remarkable PL quenching, implying efficient charge separation and suppressed carrier recombination at the heterointerface [30]. Atomic force microscope (AFM) reveals that the thicknesses of the CdS nanobelt and BiOI nanosheet are approximately 607 nm and 13 nm, respectively [Fig. 1(h)].

Figure 2(a) schematically depicts the BiOI/CdS heterojunction photodetector architecture. As shown in Fig. S5(a), a single BiOI nanosheet photodetector

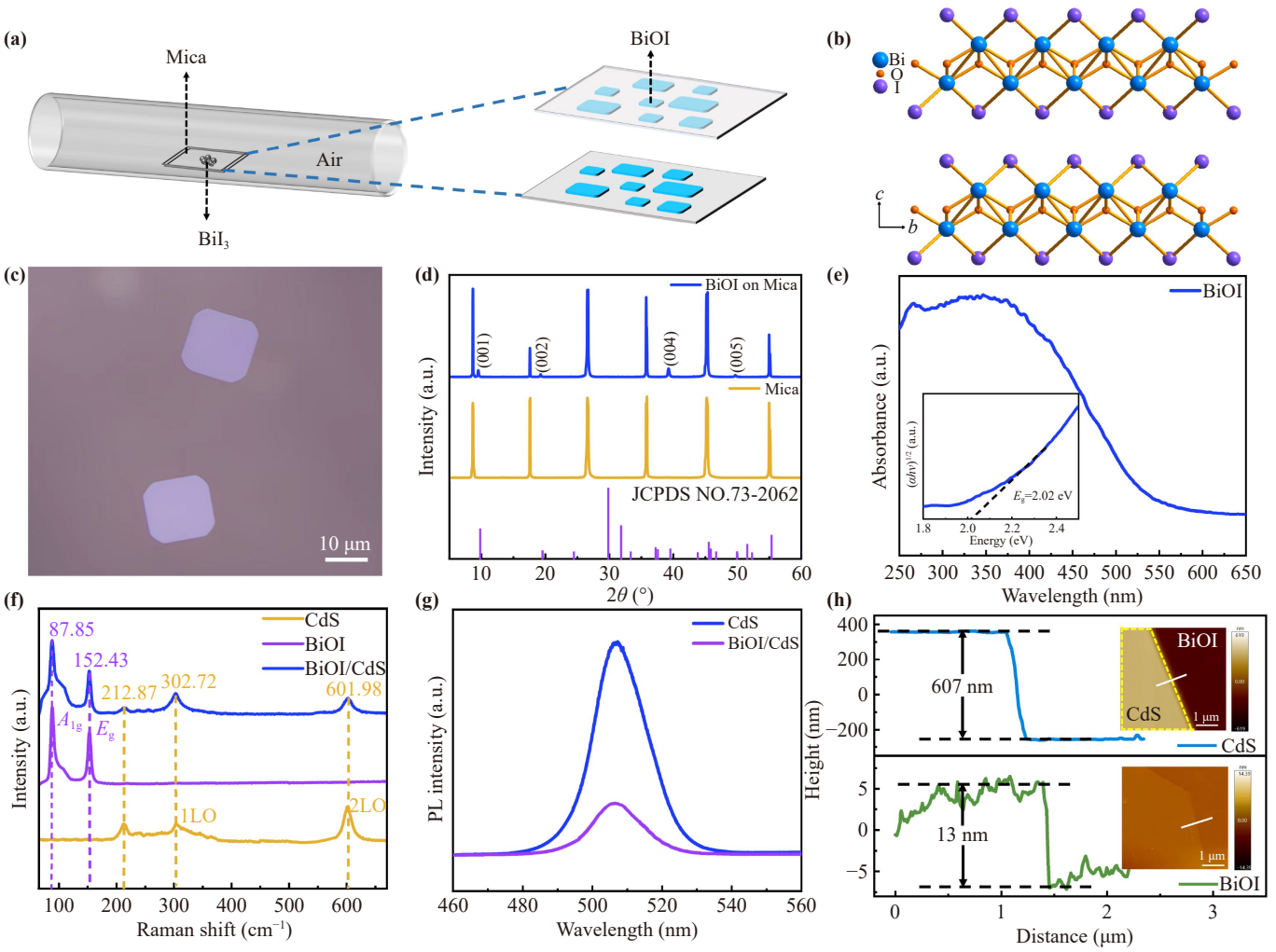

Fig. 1 **(a)** Schematic illustration of the space-confinement CVD method used for the preparation of BiOI nanosheets. **(b)** Crystal structural of the BiOI. **(c)** Optical microscopy image of the as-grown few-layer BiOI nanosheets. **(d)** XRD pattern of BiOI nanosheets grown on a mica substrate. **(e)** UV-Vis absorption spectrum of BiOI nanosheets with the corresponding optical band gap shown in the inset. **(f)** Raman spectra of BiOI, CdS, and their effectively overlapped BiOI/CdS heterojunction region. **(g)** PL spectra of CdS and the BiOI/CdS heterojunction. **(h)** AFM images of a CdS nanobelt and BiOI nanosheets.

exhibits a sharp spectral response peak at 300 nm within the 250–600 nm range. By contrast, the BiOI/CdS heterojunction [Fig. S5(b)] shows a markedly enhanced photoresponse in the UV region, with the response extending into the blue-visible range, consistent with the intrinsic optical absorption of BiOI and CdS. Based on these results, 300 nm illumination was selected for subsequent optoelectronic characterization. Under 300 nm illumination (1.280 mW/cm^2), the pristine BiOI photodetector shows a photocurrent of 5.01×10^{-10} A and a dark current of 1.2×10^{-13} A, resulting in an on/off ratio of 4.18×10^3 [Fig. S6(a)]. In contrast, the BiOI/CdS heterojunction photodetector [Fig. 2(b)] delivers a dramatically enhanced photocurrent of 1.62×10^{-5} A, while maintaining a low dark current of 8.89×10^{-13} A. Consequently, the on/off ratio reaches 1.82×10^7, approximately 4.35×10^3 times higher than that of the pristine BiOI device. Long-term environmental stability of the BiOI/CdS heterojunction device was evaluated by comparing the photocurrent under 300 nm illumination immediately after fabrication and after nine months of exposure to ambient air without encapsulation (see Fig. S7). After nine months, the device retained approximately 85% of its initial photocurrent (1.39×10^{-5} A at 1.280 mW/cm^2), indicating good stability against environmental factors such as oxygen and moisture and negligible degradation of photoelectrical performance. Figure 2(c) displays the I–V curves of the BiOI/CdS photodetector under different optical power densities at 300 nm, showing that photocurrent increases with light intensity. The relationship between photocurrent (I_{ph}) and optical power density (P) follows a power-law dependence, $I_{ph} \propto P^{\alpha}$ [Fig. 2(d)]. The fitted exponent α = 0.60, which is less than unity, suggests the existence

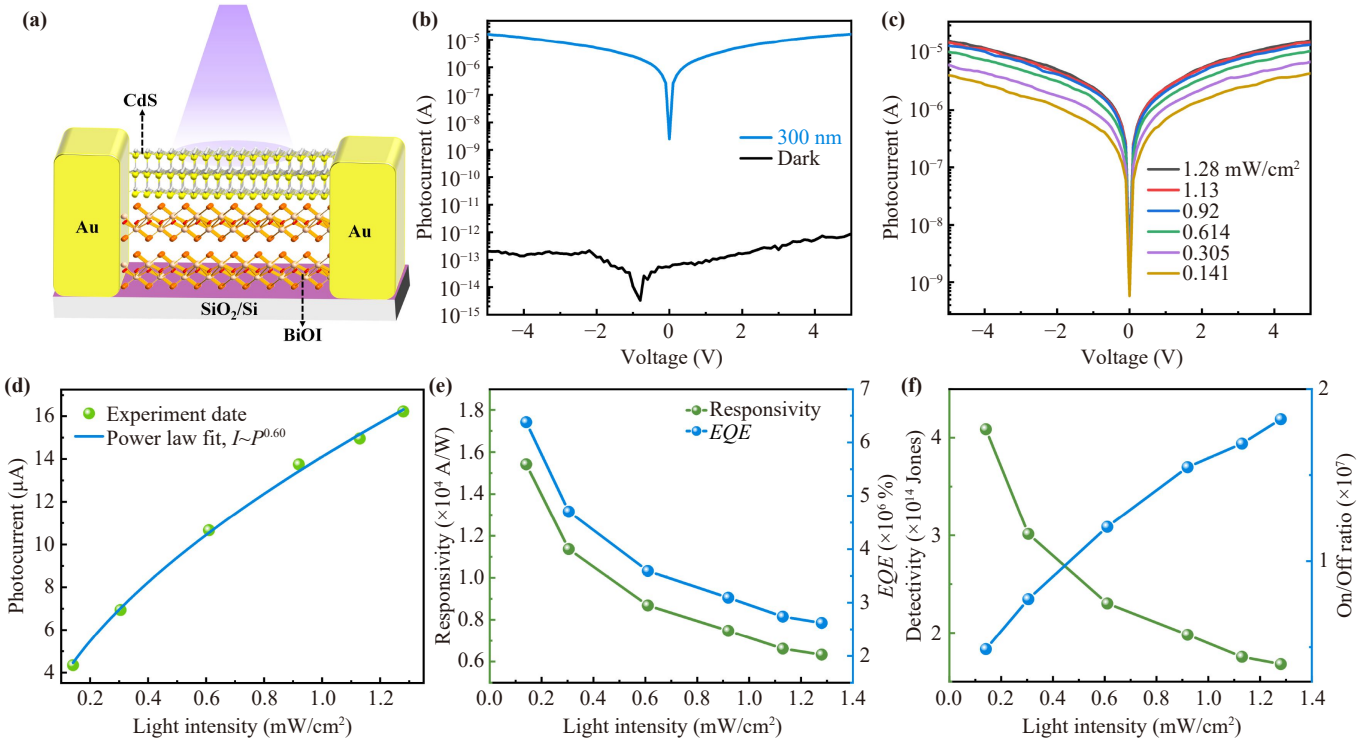

Fig. 2 **(a)** Schematic illustration of the microstructure and device configuration of the BiOI/CdS heterojunction photodetector. **(b)** Logarithmic I–V characteristics of the BiOI/CdS heterojunction photodetector measured in the dark and under 300 nm ultraviolet illumination. **(c)** Power-dependent logarithmic I–V curves of the device under 300 nm illumination. **(d)** Fitted relationship between optical power density and photocurrent. **(e)** R, EQE, and **(f)** D^* together with the on/off current ratio of the device under different optical power densities.

of trap states at the heterojunction interface that affect carrier transport [31].

The key performance metrics-responsivity (R), specific detectivity (D^*), and external quantum efficiency (EQE)-were calculated using standard equations [32, 33]:

$$R = \frac{I_{\text{ph}} - I_{\text{d}}}{PA}, \tag{1}$$

$$D^* = R\sqrt{\frac{A}{2eI_{\text{d}}}}, \tag{2}$$

$$EQE = R\frac{hc}{e\lambda}. \tag{3}$$

The results [Figs. 2(e,f)] reveal that R, D^*, and EQE gradually decrease with increasing optical power due to trap-state saturation at high illumination intensities [34]. At an optical power density of 141 μW/cm^2 and V_{ds}= 5 V, the device achieves maximum values of R= 1.54×10^4 A/W, D^*=4.08×10^{14} Jones, and EQE= 6.37×10^6 %. These results markedly outperform those of single BiOI devices [Figs. S6(c,d)], underscoring the synergistic advantages of the heterojunction configuration. The built-in electric field at the interface effectively promotes charge separation, thereby improving light detection performance and enhancing responsivity. Even at low power density (141 μW/cm^2), the on/off ratio remains as high as 4.89×10^6, confirming excellent photosensitivity. To further evaluate the performance of the BiOI/CdS heterojunction photodetectors, we measured the low-frequency noise under a 5 V bias, which exhibits typical $1/f$ behavior [Fig. S8(a)]. The frequency-dependent D^*, calculated as $D^* = \frac{R\sqrt{AB}}{I_{\text{noise}}} = \frac{R\sqrt{A}}{S_n}$ [35], where A is the active area, B is the electrical bandwidth, and S_n is the noise spectral density, remains as high as 5.95×10^{13} Jones even at 0.01 Hz [Fig. S8(b)], indicating excellent noise suppression and remarkably stable detection performance. The signal-to-noise ratio (SNR) is defined as SNR=20log(I_{i}/I_0) [36], where I_{i} and I_0 denote the measured current under illumination and in the dark, respectively, The SNR reaches 145 dB at 1.280 mW/cm^2 and remains as high as 133 dB at 0.141 mW/cm^2 (Fig. S9), demonstrating reliable SNR of the device over the measured optical intensity range.

To further verify the reliability and reproducibility of our devices, three additional BiOI/CdS heterojunction devices were refabricated using an identical preparation method, and their photoelectrical properties were systematically characterized under 300 nm illumination (V_{ds}=5 V, 1.280 mW/cm^2). As shown in Fig. S10, all devices exhibit consistently low dark current and maintain

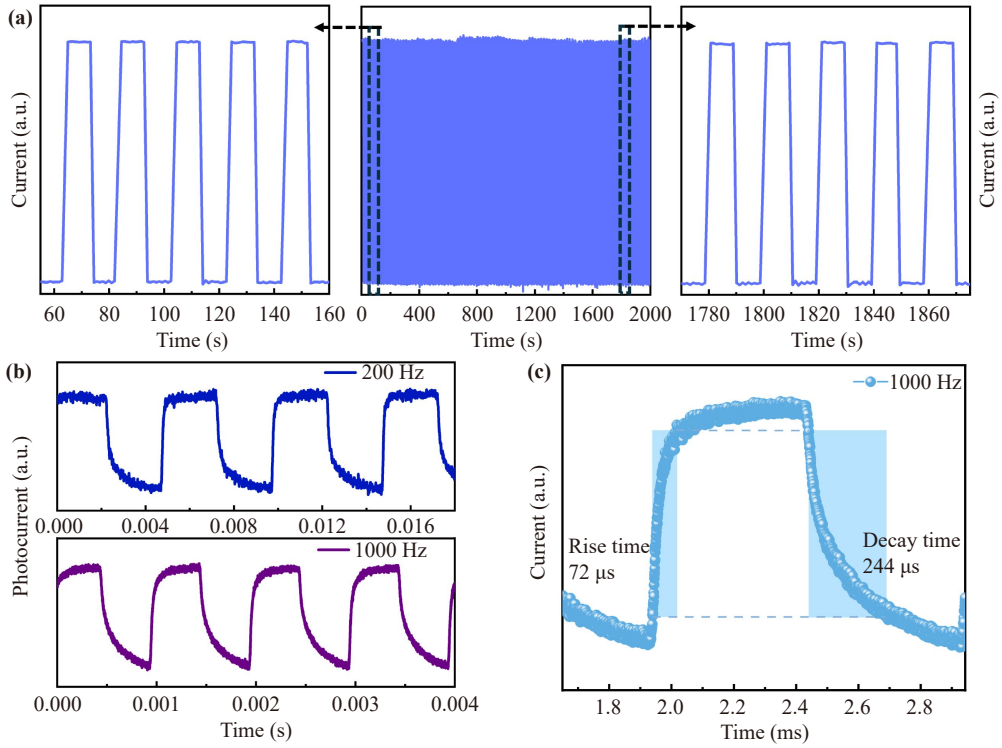

Fig. 3 **(a)** Long-term stability test of the BiOI/CdS heterojunction photodetector under continuous 300 nm ultraviolet illumination. **(b)** Time-resolved photoresponse of the device measured at different modulation frequencies. **(c)** Extracted rise and fall times of the BiOI/CdS heterojunction photodetector at a modulation frequency of 1000 Hz.

a high on/off ratio on the order of 10^7. The R and D^* of the four devices all remain within the same order of magnitude. These results confirm that the BiOI/CdS heterojunction devices demonstrate reliable reproducibility.

Device stability was evaluated through 100 continuous on/off switching cycles under 300 nm illumination [Fig. 3(a)]. The photocurrent remained nearly constant, demonstrating remarkable stability. The optical response under pulsed illumination at 200 Hz and 1000 Hz [Fig. 3(b)] reveals that the device maintains fast and stable response characteristics at various modulation frequencies [37]. From the single-cycle response at 1000 Hz [Fig. 3(c)], the rise and fall times were extracted as 72 μs and 244 μs, respectively-significantly faster than those of the pristine BiOI photodetector (Fig. S11). The rapid response behavior originates from the efficient charge generation and separation enabled by the built-in electric field in the heterojunction. Table 1 provides a systematic comparison of the performance of the BiOI/CdS heterojunction photodetector reported in this work with previously reported BiOX-based, graphene-assisted, and hybrid photodetectors. Graphene-based heterostructures typically exhibit ultrafast response speeds; however, their R and D^* are often relatively limited. In comparison, previously reported BiOX-based photodetectors generally suffer from tradeoffs among response speeds, R, and D^*, which restrict their overall performance. The BiOI/CdS heterojunction presented in this work effectively overcomes these limitations by combining strong ultraviolet absorption with a well-defined type-II band alignment. This staggered band structure promotes efficient spatial separation and directional transport of photogenerated carriers at the interface, leading to a simultaneously high R (1.54×10^4 A/W), large on/off ratio (1.82×10^7), high D^* (4.08×10^{14} Jones), and rapid response speed (72/244 μs). Compared with previously reported BiOX-based and hybrid photodetectors, the present device demonstrates a more balanced optimization of sensitivity, speed, and signal stability, underscoring the effectiveness of rational heterojunction band engineering for high-performance ultraviolet photodetection.

To elucidate the underlying operation mechanism, the interfacial potential of the BiOI/CdS heterojunction was analyzed via KPFM, as shown in Fig. 4(a). Due to differences in work function between BiOI and CdS, distinct surface potential variations emerge at the heterointerface. The potential profile [Fig. 4(b)] along the marked line indicates a potential difference of ~219.5 mV, confirming the formation of an internal electric field. The corresponding band alignment before and after contact is illustrated in Figs. 4(c) and (d), based on KPFM results and literature data [41, 49]. The system

Table 1 Comparison of key performance parameters between BiOI/CdS devices and photodetectors based on BiOX and graphene.

Device	V_{ds} (V), λ (nm)	R (A·W^{-1})	D^* (Jones)	On/Off	τ_{rise}/τ_{fall} (ms)	Ref.
BiOI (001) film	–10, 450	0.0435	8.7×10^{10}	30	20.7/22.3	[14]
BiOI nanosheet	10, 473	0.026	8.2×10^{11}	1×10^{5}	120/250	[15]
P$^+$-FLG/ n$^-$-ZnO NWs	0, 350	0.12	1.9×10^{9}	2.5×10^{5}	0.26×10^{-6}/ 0.26×10^{-6}	[17]
Au-BiOI	2, 533	1.42	–	1.65×10^{2}	–	[38]
CuSe@BiOI	–, 420	0.08713	6.97×10^{11}	–	4.4/53.4	[39]
BiOI/WO_3	0 , 370	0.0081	9.1×10^{8}	–	–	[40]
BiOI (102) film	0, 420	0.07833	4.61×10^{11}	–	–	[41]
BiOI nanosheet	10, 310	1.048	4.7×10^{12}	~10^2	0.42/0.69	[42]
Bulk BiOBr	10, 334	6.3	3.2×10^{9}	~10	257/1964	[43]
6-BiOCl-TiO_2	–5, 350	41.94	1.41×10^{14}	2.23×10^{5}	12900/810	[44]
TiO_2/BiOCl/PEDOS	0, 365	0.1088	3.93×10^{11}	–	80.2/79.8	[45]
BiOBr	8, 365	12.4	1.6×10^{13}	~10^2	551/2416	[46]
BiOCl/TiO_2	0, 340	0.17	1.3×10^{12}	10^3	23/860	[47]
P$^+$-BLG/n$^+$-ZnO NWs	–0.5, 350	0.16	2.44×10^{9}	16.25	0.17×10^{-6}/ 0.17×10^{-6}	[48]
BiOI/CdS	5, 300	1.54×10^{4}	4.08×10^{14}	1.82×10^{7}	0.072/0.244	This work

forms a typical type-II heterojunction in which CdS, possessing a higher Fermi level before contact, transfers electrons to BiOI upon junction formation until Fermi level equilibrium is achieved, resulting in band bending and the generation of an internal electric field directed from CdS to BiOI [50, 51]. Under UV illumination, photons with energy exceeding both bandgaps generate electron–hole pairs in BiOI and CdS. The built-in field drives electrons from BiOI's conduction band to that of CdS and holes from CdS's valence band to BiOI's valence band, promoting spatial charge separation and minimizing recombination. The spatial photocurrent mapping results [Figs. 4(e,f)] further validate this mechanism. Under 405 nm laser excitation (V_{ds}=5 V), the strongest photocurrent signals appear precisely in the heterojunction overlap region, confirming that the junction serves as the active center for carrier generation and separation. To clarify the origin of the exceptionally high R and EQE, we further analyze the bias-dependent photoresponse, as shown in Fig. S12. The nearly linear dependence of photocurrent on bias voltage, together with the microsecond-scale response speed [Fig. 3(c)], excludes a dominant trap-assisted photogating mechanism and supports a photoresponse governed by efficient carrier separation and transport enabled by the type-II heterojunction.

To further investigate the image-sensing capabilities of the BiOI/CdS heterojunction photodetector, a single-pixel scanning imaging system was employed, whose schematic is illustrated in Fig. 5(a). A 295 nm laser was directed through a mask patterned with the letter "U" onto the heterojunction photodetector. By precisely moving the mask along the x- and y-axes, the corresponding photocurrent values were recorded using a semiconductor parameter analyzer. These photocurrent values were then compiled and converted into a high-resolution image of the letter "U" [Fig. 5(b)] based on their spatial coordinates. The clear recognition of the "U" pattern demonstrates the high photosensitivity and imaging potential of the BiOI/CdS heterojunction-based system. Furthermore, this study has successfully demonstrated ultraviolet communication utilizing a 300 nm laser based on a BiOI/CdS heterojunction. Figure 5(c) illustrates the schematic diagram of the BiOI/CdS heterojunction device within the ultraviolet communication system. As shown in Fig. 5(d), a voltage signal representing the ASCII code "UWHY" was applied to the laser via a signal generator to modulate the laser emission. Upon receiving the optical signal, the BiOI/CdS heterojunction photodetector generated a corresponding photocurrent signal that accurately reflected the ASCII code "UWHY", as depicted in Fig. 5(e). This output current signal could be further processed and decoded to retrieve the original message "UWHY", thereby confirming the feasibility of ultraviolet communication based on this heterojunction device.

4 Conclusion

In summary, a high-performance photodetector based on a BiOI nanosheet/CdS nanobelt heterojunction was successfully fabricated. The device exhibits an impressive switching current ratio of 1.82×10^7 and rapid response times of 72 μs (rise) and 244 μs (fall). Under 300 nm ultraviolet illumination, the photodetector demonstrates

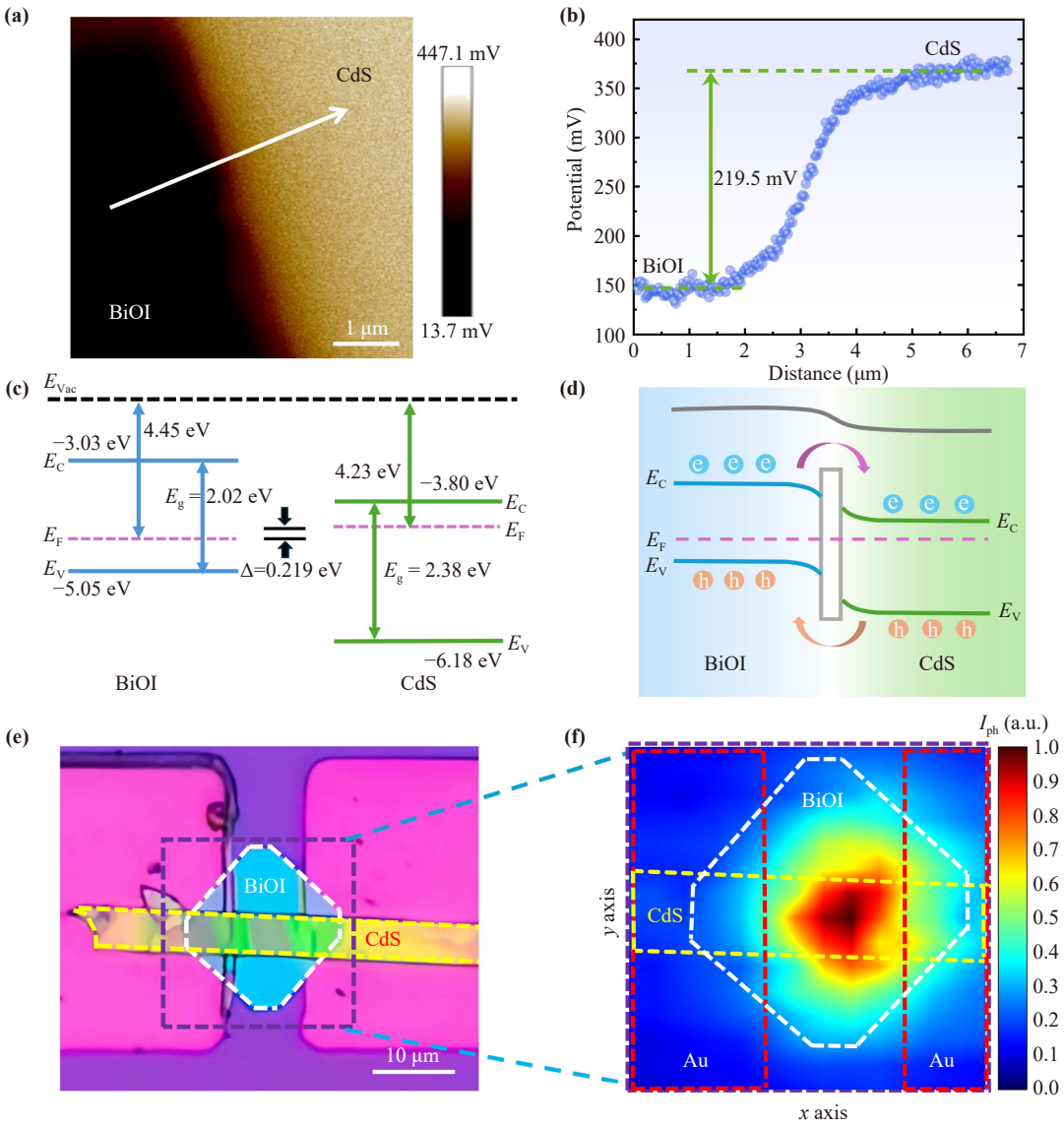

Fig. 4 **(a)** KPFM surface potential mapping of the BiOI/CdS heterojunction. **(b)** Corresponding contact potential difference profile across the BiOI/CdS interface. **(c)** Energy band structure of BiOI and CdS before contact. **(d)** Schematic energy band alignment of the BiOI/CdS heterojunction after contact under illumination. **(e)** Optical microscopy image of the fabricated BiOI/CdS heterojunction device. **(f)** Scanning photocurrent mapping of the BiOI/CdS device under 405 nm laser illumination, where the white and yellow dashed regions correspond to BiOI and CdS, respectively

outstanding optoelectronic properties, including a high responsivity of 1.54×10^4 A/W, an external quantum efficiency of up to 6.37×10^6%, and a specific detectivity of 4.08×10^{14} Jones. The superior performance of the device originates from the typical type-II band alignment and the strong built-in electric field established at the BiOI/CdS heterointerface, which together facilitate efficient charge separation and suppress carrier recombination. Moreover, the BiOI/CdS heterojunction photodetector was successfully applied to ultraviolet imaging and optical communication, demonstrating its excellent stability, sensitivity, and functional versatility. This work not only offers valuable insights into the rational design of bismuth-based semiconductor optoelectronic devices but also highlights the great potential of BiOI/CdS heterostructures for next-generation ultraviolet photodetection and communication technologies.

Declarations The authors declare that they have no competing interests and that there are no conflicts.

Electronic supplementary materials The online version contains supplementary material available at https://doi.org/10.15302/frontphys.2026.114202.

Acknowledgements This work was supported by the National

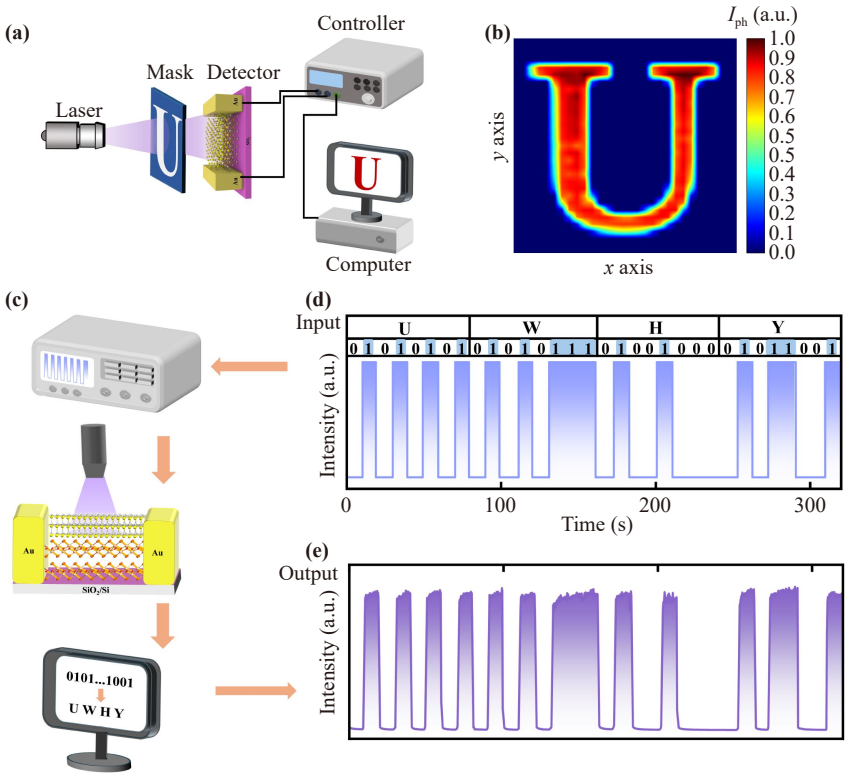

Fig. 5 **(a)** Schematic illustration of the single-pixel scanning imaging system. **(b)** Reconstructed image of the letter "U" pattern obtained under 295 nm ultraviolet illumination. **(c)** Schematic diagram of the BiOI/CdS heterojunction device integrated into the ultraviolet optical communication system. **(d)** Applied voltage signal corresponding to the ASCII code "UWHY". **(e)** Recorded output photocurrent signal of the BiOI/CdS heterojunction photodetector reproducing the transmitted information.

Natural Science Foundation of China (Nos. 62464014, 12464025, and 12264056), the Basic Research Program of Yunnan Province (No. 202401AT070134), the Project for Building a Science and Technology Innovation Center Facing South Asia and Southeast Asia (No. 202403AP140015), and the Spring City Plan: The High-level Talent Promotion and Training Project of Kunming (No. 2022SCP005).

References

1. Y. Wang, L. Mei, Y. Li, X. Xia, N. Cui, G. Long, W. Yu, W. Chen, H. Mu, and S. Lin, Integration of two-dimensional materials based photodetectors for on-chip applications, *Phys. Rep.* 1081, 1 (2024)
2. J. Han, Z. Fu, J. Wei, S. Han, W. Deng, F. Hu, Z. Wang, H. Zhou, H. Yu, J. Gou, and J. Wang, 2D materials-based next-generation multidimensional photodetectors, *Light Sci. Appl.* 14(1), 362 (2025)
3. Z. Meng, Z. Jiang, Y. Zheng, K. Shi, J. Li, X. Pan, and F. Liu, Self-powered photodetectors based on transition-metal dichalcogenides: A heterojunction perspective, *Front. Phys. (Beijing)* 20(5), 054301 (2025)
4. J. Chu, F. Wang, L. Yin, L. Lei, C. Yan, F. Wang, Y. Wen, Z. Wang, C. Jiang, L. Feng, J. Xiong, Y. Li, and J. He, High-performance ultraviolet photodetector based on a few-layered 2D $NiPS_3$ nanosheet, *Adv. Funct. Mater.* 27(32), 1701342 (2017)
5. J. Chen, L. Li, P. Gong, H. Zhang, S. Yin, M. Li, L. Wu, W. Gao, M. Long, L. Shan, F. Yan, and G. Li, A submicrosecond-response ultraviolet-visible-near-infrared broadband photodetector based on 2D tellurosilicate $InSiTe_3$, *ACS Nano* 16(5), 7745 (2022)
6. W. Wang, Y. Meng, Y. Zhang, Z. Zhang, W. Wang, Z. Lai, P. Xie, D. Li, D. Chen, Q. Quan, D. Yin, C. Liu, Z. Yang, S. Yip, and J. C. Ho, Electrically switchable polarization in Bi_2O_2Se ferroelectric semiconductors, *Adv. Mater.* 35(12), 2210854 (2023)
7. H. Wang, B. Zhang, Y. Tang, C. Wang, F. Zhao, and B. Zeng, Recent advances in bismuth oxyhalide-based functional materials for photoelectrochemical sensing, *Trends Analyt. Chem.* 131, 116020 (2020)
8. L. Lu, H. Zhang, Z. Sun, J. Wang, H. Wang, J. Xue, Q. Shen, and Q. Li, Creation of robust oxygen vacancies in 2D ultrathin BiOBr nanosheets by irradiation through photocatalytic memory effect for enhanced CO_2 reduction, *Chem. Eng. J.* 477, 146892 (2023)
9. F. Huang, Y. Liu, F. Wang, Y. Liu, and L. Guo, Crystal defects engineering of BiOI elevated photocatalytic CO_2 to C_2 conversion performance, *Sci. China Mater.* 68(5), 1561 (2025)
10. P. Lei, H. Duan, L. Qin, X. Wei, R. Tao, Z. Wang, F. Guo, M. Song, W. Jie, and J. Hao, High-performance memristor based on 2D Layered BiOI nanosheet for low-

power artificial optoelectronic synapses, *Adv. Funct. Mater.* 32(25), 2201276 (2022)
11. C. Gong, J. Chu, S. Qian, C. Yin, X. Hu, H. Wang, Y. Wang, X. Ding, S. Jiang, A. Li, Y. Gong, X. Wang, C. Li, T. Zhai, and J. Xiong, Large-scale ultrathin 2D wide-bandgap BiOBr nanoflakes for gate-controlled deep-ultraviolet phototransistors, *Adv. Mater.* 32(12), 1908242 (2020)
12. Q. Zhang, T. Duan, M. Xiao, Y. Pei, X. Wang, C. Zhi, X. Wu, B. Long, and Y. Wu, BiOI nanopaper as a high-capacity, long-life and insertion-type anode for a flexible quasi-solid-state Zn-ion battery, *ACS Appl. Mater. Interfaces* 14(22), 25516 (2022)
13. Z. Y. Zhao, and W. W. Dai, Structural, electronic, and optical properties of Eu-doped BiOX (X = F, Cl, Br, I): A DFT+U study, *Inorg. Chem.* 53(24), 13001 (2014)
14. Z. Sun, Y. Wang, and B. Mei, Highly sensitive UV photodetector based on solution-processed bismuth oxyiodide epitaxial thin films, *J. Mater. Chem. C* 11(11), 3805 (2023)
15. W. Zeng, J. Li, L. Feng, H. Pan, X. Zhang, H. Sun, and Z. Liu, Synthesis of large-area atomically thin BiOI crystals with highly sensitive and controllable photodetection, *Adv. Funct. Mater.* 29(16), 1900129 (2019)
16. S. Bansal, A. Das, K. Prakash, K. Sharma, G. M. Khanal, N. Sardana, S. Kumar, N. Gupta, and A. K. Singh, Bilayer graphene/HgCdTe heterojunction based novel GBn infrared detectors, *Micro Nanostructures* 169, 207345 (2022)
17. S. Bansal, S. Kumar, A. Jain, V. Rohilla, K. Prakash, A. Gupta, T. Ali, A. M. Alenezi, M. S. Islam, M. S. Soliman, and M. T. Islam, Design and TCAD analysis of few-layer graphene/ZnO nanowires heterojunction-based photodetector in UV spectral region, *Sci. Rep.* 15(1), 7762 (2025)
18. S. Bansal, Long-wave bilayer graphene/HgCdTe based GBp type-II superlattice unipolar barrier infrared detector, *Results in Optics* 12, 100425 (2023)
19. Z. Zheng, Y. Qiao, Y. Cai, Y. He, Y. Tang, and L. Li, MoS_2 decorated CdS hybrid heterojunction for enhanced photoelectrocatalytic performance under visible light irradiation, *J. Colloid Interface Sci.* 533, 561 (2019)
20. N. V. Hullavarad, S. S. Hullavarad, and P. C. Karulkar, Cadmium sulphide (CdS) nanotechnology: synthesis and applications, *J. Nanosci. Nanotechnol.* 8(7), 3272 (2008)
21. M. Z. Nawaz, L. Xu, X. Zhou, K. H. Shah, J. Wang, B. Wu, and C. Wang, CdS nanobelt-based self-powered flexible photodetectors with high photosensitivity, *Mater. Adv.* 2(18), 6031 (2021)
22. D. Dai, J. Qiu, G. Xia, L. Zhang, H. Ma, L. Yang, and J. Yao, Interspersing CdS nanodots into iodine vacancy-rich BiOI sphere for photocatalytic lignin valorization, *Int. J. Biol. Macromol.* 227, 1317 (2023)
23. S. Wang, Y. Chen, L. Li, Y. Long, Y. Shi, Y. Zhang, and F. Jiang, Preparation and characterization of CdS/BiOI composites with enhanced photocatalytic activity for degradation of 17α-ethinyl estradiol, *Mater. Res. Bull.* 99, 444 (2018)
24. Z. Fu, C. Jian, Y. Yao, Y. Li, J. Yuan, Q. Cai, and W. Liu, Low-temperature controlled growth of 2D LaOCl with enhanced dielectric properties for advanced electronics, *Adv. Funct. Mater.* 35(34), 2501136 (2025)
25. X. Li, F. Cui, Q. Feng, G. Wang, X. Xu, J. Wu, N. Mao, X. Liang, Z. Zhang, J. Zhang, and H. Xu, Controlled growth of large-area anisotropic ReS_2 atomic layer and its photodetector application, *Nanoscale* 8(45), 18956 (2016)
26. N. Mounet, M. Gibertini, P. Schwaller, D. Campi, A. Merkys, A. Marrazzo, T. Sohier, I. E. Castelli, A. Cepellotti, G. Pizzi, and N. Marzari, Two-dimensional materials from high-throughput computational exfoliation of experimentally known compounds, *Nat. Nanotechnol.* 13(3), 246 (2018)
27. X. Yang, L. Qu, F. Gao, Y. Hu, H. Yu, Y. Wang, M. Cui, Y. Zhang, Z. Fu, Y. Huang, W. Feng, B. Li, and P. Hu, High-performance broadband photoelectrochemical photodetectors based on ultrathin Bi_2O_2S nanosheets, *ACS Appl. Mater. Interfaces* 14(5), 7175 (2022)
28. L. Ye, L. Tian, T. Peng, and L. Zan, Synthesis of highly symmetrical BiOI single-crystal nanosheets and their {001} facet-dependent photoactivity, *J. Mater. Chem.* 21(33), 12479 (2011)
29. W. Zeng, L. Feng, J. Li, H. Pan, X. Zhang, X. Zheng, Y. Huang, R. Zhang, and Z. Liu, Synthesis of millimeter-size single-crystal 2D BiOI sheets and ribbons on mica, *Chem. Mater.* 31(23), 9715 (2019)
30. Y. Wang, C. Du, P. Li, Y. Yang, Y. Xiao, T. Ge, X. Jiang, Y. Liu, H. Gao, K. Li, and W. Wang, Photodetectors based on ZrS_3/MoS_2 heterostructures, *ACS Appl. Mater. Interfaces* 16(22), 29049 (2024)
31. L. Li, H. Li, J. Li, H. Wu, L. Yang, W. Zhang, and H. Chang, Chemical vapor deposition-grown nonlayered α-MnTe nanosheet for photodetectors with ultrahigh responsivity and external quantum efficiency, *Chem. Mater.* 33(1), 338 (2021)
32. R. Ma, Q. Tan, P. Yang, Y. Liu, and Q. Wang, High performance photodetector based on few-layer $MoTe_2/CdS_{0.42}Se_{0.58}$ flake heterojunction, *Front. Phys. (Beijing)* 19(4), 43204 (2024)
33. X. Pan, Z. Xu, J. Li, K. Shi, M. Xu, X. Fang, and G. Qu, Defect control during CVD-growth for high performance MoS_2-based self-powered photodetector, *Front. Phys. (Beijing)* 20(2), 024206 (2025)
34. B. Liu, Y. Sun, Y. Wu, K. Liu, H. Ye, F. Li, L. Zhang, Y. Jiang, and R. Wang, Enhanced photoresponse of TiO_2/MoS_2 heterostructure phototransistors by the coupling of interface charge transfer and photogating, *Nano Res.* 14(4), 982 (2021)
35. N. Huo, and G. Konstantatos, Recent progress and future prospects of 2D-based photodetectors, *Adv. Mater.* 30(51), 1801164 (2018)
36. Y. He, Z. Han, J. Li, Y. Gu, Y. Zou, Y. Wang, J. Yang, W. Lei, and X. Xu, Sensitive filter-free narrowband infrared photodetectors for weak light detection and ranging, *Laser Photonics Rev.* 18(9), 2300791 (2024)
37. Y. Wang, Z. Lai, S. Tang, J. Wang, Q. Zhou, S. Li, W. Wang, H. Zhao, Y. Yu, and L. Gao, $ReS_2/MoSe_2$ van der Waals heterostructure photodetectors for polarization imaging and polarization-encoded optical communication, *Small* 21(34), 2503599 (2025)
38. M. D. Prasad, M. G. Krishna, and S. K. Batabyal, Facet-engineered surfaces of two-dimensional layered

BiOI and Au–BiOI substrates for tuning the surface-enhanced Raman scattering and visible light photodetector response, *ACS Appl. Nano Mater.* 2(6), 3906 (2019)
39. X. Gong, S. Fan, Q. Yang, J. L. Yang, Y. chen, X. Qi, H. Shen, D. Ren, and M. Wang, Porous two-dimensional CuSe@BiOI isotype heterojunction with highly exposed (102) facets for efficient photoelectrocatalytic CO_2 reduction and photodetection, *Chem. Eng. J.* 493, 152773 (2024)
40. F. Liu, J. Xu, S. Shi, J. Li, C. Pang, L. Kong, X. Zhang, and L. Li, Bidirectionally regulated ultraviolet and visible dual-band photoresponse characteristics of self-powered BiOI/WO_3 photodetectors, *Adv. Opt. Mater.* 12(30), 2401244 (2024)
41. Z. Sun, H. Zhang, and B. Mei, Enhanced charge separation and transfer efficiency of BiOI with the dominantly exposed (102) facet for sensitive photoelectrochemical photodetection, *Inorg. Chem.* 62(14), 5512 (2023)
42. Y. Li, Z. Fu, B. Wang, Y. Yao, J. Yuan, M. Li, X. He, and W. Liu, Synthesis of large-area high quality 2D BiOI for highly sensitive ultraviolet photodetection, *J. Mater. Chem. C* 12(19), 6826 (2024)
43. C. Zhang, L. Lin, J. Song, L. Lei, L. Han, Y. Liu, J. Zhang, Z. Zheng, Z. Wang, P. Wang, H. Cheng, Y. Dai, and B. Huang, Growth of bulk BiOBr single crystals for the characterization of intrinsic semi-conductive properties and application in ultraviolet photodetectors, *J. Mater. Chem. C* 10(28), 10330 (2022)
44. W. Ouyang, F. Teng, and X. Fang, High performance BiOCl nanosheets/TiO_2 nanotube arrays heterojunction UV photodetector: The influences of self-induced inner electric fields in the BiOCl nanosheets, *Adv. Funct. Mater.* 28(16), 1707178 (2018)
45. X. Tang, T. Abdiryim, R. Jamal, X. Liu, F. Liu, F. Xu, A. Abdurexit, N. Serkjan, S. Xie, and Y. Liu, Pyro-phototronic effect enhanced the performance of TiO_2 NRs/BiOCl/PEDOS heterojunction for a UV photodetector, *Chem. Eng. J.* 488, 150940 (2024)
46. P. Liu, L. Yin, L. Feng, Y. Sun, H. Sun, W. Xiong, C. Xia, Z. Wang, and Z. Liu, Controllable preparation of ultrathin 2D BiOBr crystals for high-performance ultraviolet photodetector, *Sci. China Mater.* 64(1), 189 (2021)
47. Q. Zhang, J. Xu, M. Li, J. Chen, J. Xu, Q. Zheng, S. Shi, L. Kong, X. Zhang, and L. Li, High-performance self-powered ultraviolet photodetector based on BiOCl/TiO_2 heterojunctions: Carrier engineering of TiO_2, *Appl. Surf. Sci.* 592, 153350 (2022)
48. S. Bansal, K. Prakash, K. Sharma, N. Sardana, S. Kumar, N. Gupta, and A. K. Singh, A highly efficient bilayer graphene/ZnO/silicon nanowire based heterojunction photodetector with broadband spectral response, *Nanotechnology* 31(40), 405205 (2020)
49. Q. Zhang, Q. Tan, J. Ding, X. Feng, P. Yang, Y. Liu, and Q. Wang, High performance dual-band Bi_2O_2Se/CdS heterojunction photodetector for encrypted optical communication, *Nano Res.* 18(8), 94907550 (2025)
50. J. Zhou, W. Chen, L. Lu, B. Zhu, G. Ren, Y. Pan, J. Ou, and L. Zhu, Interlayer transition induced infrared response in WSe_2/WS_2 van Der Waals heterostructure photodetectors with polarization and self-powered effects, *Adv. Opt. Mater.* 13(12), 2403253 (2025)
51. G. Wang, Z. Sa, Z. Zang, P. Li, M. Wang, B. Yang, X. Wang, Y. Yin, and Z. X. Yang, Mixed-dimensional nanowires/nanosheet heterojunction of GaSb/Bi_2O_2Se for self-powered near-infrared photodetection and photocommunication, *Nano-Micro Lett.* 17(1), 284 (2025)